

OBSERVATIONAL AND SIMULATION-BASED INSIGHTS INTO ATTITUDE DYNAMICS OF LARGE ROCKET DEBRIS FOR ACTIVE DEBRIS REMOVAL

Hiroyuki Okamoto⁽¹⁾, Yuki Ikeda⁽¹⁾, Moeko Hidaka⁽¹⁾, Daichi Hirano⁽¹⁾, Shinji Mitani⁽¹⁾, Toru Yamamoto⁽¹⁾, Lars Fuhrmann⁽²⁾, Frank Schlichthaber⁽²⁾, Taro Kashiwayanagi⁽³⁾

⁽¹⁾ Japan Aerospace Exploration Agency, 2-1-1 Sengen, Tsukuba, Ibaraki 305-8505, Japan,
Email: okamoto.hiroyuki@jaxa.jp

⁽²⁾ Fraunhofer Institute for High Frequency Physics and Radar Techniques FHR, Fraunhoferstraße 20, 53343 Wachtberg, Germany

⁽³⁾ Astroscale Japan Inc., 4-17-1 Kinshi, Sumida, Tokyo, 130-0013, Japan

ABSTRACT

The Commercial Removal of Debris Demonstration (CRD2) project, led by JAXA, deployed the ADRAS-J spacecraft to rendezvous within 50 meters of a spent H-IIA upper stage, capturing images to study its attitude motion. Complementary radar observations by the FHR TIRA system analyzed multiple H-IIA upper stages, revealing a consistent gravity-gradient-stabilized attitude with engine sides oriented toward zenith. Numerical simulations incorporating J_2 gravitational harmonics and solar radiation pressure (SRP) torques partially explain this orientation and observed pitch (1-1.5°) and roll (~2°) librations, though discrepancies with observational data suggest unmodeled factors. These findings enhance our understanding of debris dynamics for Active Debris Removal (ADR) mission planning.

1 INTRODUCTION

Space activities are intensifying, and the need to preserve the space environment is becoming increasingly critical. Several strategies exist to maintain the space environment, with Active Debris Removal (ADR) of large debris recognized as an effective method.[1]

ADR involves approaching and capturing target debris, where the attitude motion of the debris plays a pivotal role. The attitude motion of large debris in orbit is assumed to exhibit significant variation.

Ground-based observations, such as those utilizing optical telescopes or imaging radar, provide valuable insights into the properties of both rotating and stationary objects. Certain studies have concentrated on analyzing the attitude motion of debris through light curves derived from photometric measurements, which have proven effective in classifying debris as either fast-rotating or slowly tumbling objects.

Ikeda, N., et al. used MU radar data and tried to obtain the attitude motion parameters.[2] One of their measurements is a H-IIA rocket body orbiting LEO, and

they found difficulties to obtain the attitude motion parameters.

Silha, J., et al. presents findings from the ESA project "Debris Attitude Motion Measurements and Modelling" (ESA AO/1-7803/14/D/SR), dedicated to determining the attitude motion of large spacecraft and upper stages.[3] The study integrates passive optical observations, laser ranging, and radar data, with two primary objectives: rapid determination of the attitude motion vector in contingency scenarios and long-term (e.g., 10 years) prediction of spin rates for ADR missions. A key component is the development of the iOTA (In-Orbit Tumbling Analysis) software tool, which performs short- to long-term propagations of orbit and attitude motion, accounting for perturbations like gravity, solar radiation pressure, and atmospheric drag. The tool generates synthetic measurements, such as light curves and SLR residuals, validated through coordinated observation campaigns on four priority targets.

Rodriguez-Villamizar, J., et al. provides an update on ground-based observations conducted at the Swiss Optical Ground Station and Geodynamics Observatory (SwissOGS) near Bern, Switzerland.[4] Operated by the Astronomical Institute of the University of Bern, SwissOGS maintains a database of synodic periods estimated from light curves of resident space objects. The study focuses on recent observations, likely discussing improvements in data collection and analysis, and their implications for understanding the attitude and motion of space debris. This work contributes to the growing need for precise data in support of ADR and collision avoidance strategies.

Zhao, S., et al. details the application of Satellite Laser Ranging (SLR) and light curve data, measured with a single-photon detector at Graz station, to derive attitude parameters of rocket bodies, a major contributor to space debris.[5] Focusing on the CZ-3B R/B (NORAD ID 38253), the study combines the epoch method with light curve and SLR residuals fitting to deduce the spin axis

and period. This approach addresses the challenges of uncooperative targets, providing a reference for attitude determination methods essential for debris removal and collision avoidance missions, enhancing space safety.

Isoletta, G., et al. proposes a method for classifying the attitude motion of Earth-orbiting objects using spectral analysis of light curves, crucial for Space Domain Awareness.[6] Light curves, which graph brightness variations over time, are analyzed to infer dynamical and physical properties, addressing challenges like measurement noise and data gaps. The method leverages frequency spectra to identify different motion types, such as tumbling, offering a robust approach for characterizing space debris behavior, with implications for mission planning and safety.

Direct observations using Earth observation satellite sensors have captured images of space debris, some of which are publicly available.[7] However, due to the vast distance between the sensor and the debris, analyzing precise attitude motion from these images remains challenging.

Japan Aerospace Exploration Agency (JAXA) is developing a novel Active Debris Removal (ADR) technology that involves rendezvousing with uncooperative client debris, followed by capture and deorbiting operations. This system employs a highly efficient propulsion system integrated into the ADR spacecraft. To evaluate the technological feasibility of ADR systems, JAXA initiated the Commercial Removal of Debris Demonstration (CRD2) project.[8] The CRD2 project is structured in two phases: Phase 1 focuses on rendezvousing with and imaging an uncooperative client, while Phase 2 encompasses the rendezvous, capture, and deorbiting of large debris. The target debris for CRD2 was selected from Japan's rocket upper stages, specifically the H-IIA upper stage that launched GOSAT in 2009. At the time of selection, limited data on its attitude motion were available, primarily from numerical simulations.

The Fraunhofer Institute for High Frequency Physics and Radar Techniques (FHR) operates the Tracking and Imaging Radar (TIRA), which employs inverse synthetic aperture radar (ISAR) techniques to generate ground-based radar images and image sequences for estimating the attitude motion of space objects.[9][10] JAXA collaborated with FHR to observe the client debris for CRD2 Phase 1, with TIRA conducting observations over three years.

The CRD2 Phase 1 spacecraft, named ADRAS-J, was developed and operated by Astroscale Japan.[11] ADRAS-J approached the spent H-IIA upper stage and captured still images using an onboard optical camera. By analyzing multiple images, the attitude motion of the debris was estimated.

In prior work,[12] the debris attitude simulation results were compared with observations from ADRAS-J images and FHR radar data. The in-plane attitude motion of the H-IIA upper stage was analyzed, revealing that orbital eccentricity is the primary perturbation parameter affecting in-plane libration. While out-of-plane libration was also observed in the ADRAS-J images, this behavior could not be attributed to orbital eccentricity.

In this study, the mechanisms driving out-of-plane libration and the stabilized orientation of the H-IIA upper stage—specifically its engine-side-to-zenith alignment—are investigated using on-orbit images, ground-based radar observations, and numerical simulations.

2 CRD2 PHASE1 RESULT

2.1 ADRAS-J result and images

ADRAS-J was launched on 18. Feb. 2024 by Electron rocket of Rocket Lab from Launch Complex 1, New Zealand. After orbital insertion, ADRAS-J rendezvoused to the H-IIA upper stage using several navigation's means, i.e. GPS absolute navigation, Angles Only Navigation (AON), and Model Matching Navigation (MMN). Finally, ADRAS-J was approaching the H-IIA upper stage within 50 m distance and obtaining optical images.

A fixed-point observation, during which the relative position remained stable for one full orbit, was conducted approximately 50 meters behind the H-IIA upper stage. ADRAS-J carried out three fixed-point observations. Figure 1 illustrates the positional relationship between ADRAS-J and the H-IIA upper stage, while Figure 2 provides a representative example of an image captured during one such observation. Following the fixed-point observations, fly-around observations were performed three times. During the fly around observations, ADRAS-J maintained a consistent distance of 50 meters from the debris and orbited around it within one orbital period. Throughout both the fixed-point and fly-around observations, ADRAS-J captured similar images at 24-second intervals. These sequential images are utilized as input data for the motion estimation process.

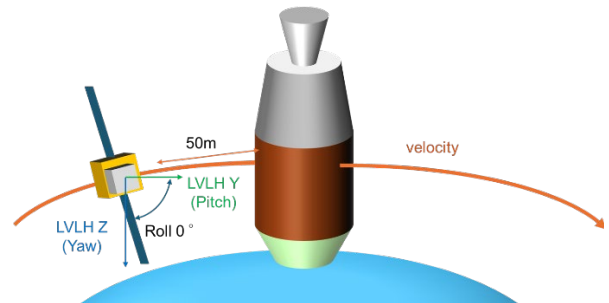


Figure 1 Illustrate of the Fixed point observation

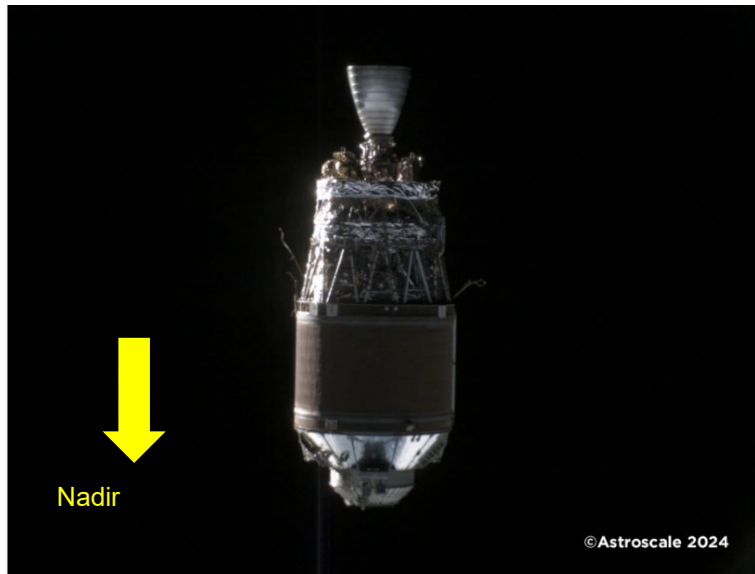


Figure 2 Fixed Point Observation Image
 Image captured on 2024/5/23 4:32:52 at distance of $R = 0.35$ m, $I = -49.3$ m, and $C = -0.28$ m. ADRAS-J attitude to LVLH is roll = -0.00933° , pitch = -0.624° , and yaw = 0.416° .

2.2 Motion Estimation using Manual Matching Technology

To determine the debris' attitude from ADRAS-J images, JAXA developed a manual matching method—a vision-based technique where human operators assist in aligning a 3D model with observed images. This approach, detailed in Hidaka et al. (2023) [13], addresses challenges posed by sunlight reflections and shadows, which can obscure automatic feature detection in optical images.

The process begins with an operator examining each image and identifying key feature points on the debris, such as edges of the Payload Attachment Fitting (PAF) or engine nozzle. These points are predefined based on the H-IIA upper stage's known geometry. Next, the Perspective-n-Point (PnP) problem is solved mathematically to estimate the debris' position and attitude relative to the camera, using the spatial relationships between the selected points. A wireframe of the debris model is then overlaid on the image, as shown in Figure 3, and the operator fine-tunes its alignment by adjusting the wireframe to match the observed outline. This refinement ensures accuracy despite visual noise. The output includes a quaternion (describing the rotation from the camera frame to the debris frame) and a position vector (from the camera's origin to the debris' center).

For an axisymmetric object like the H-IIA upper stage, feature points are chosen to capture motion in all three axes—roll (around the long axis), pitch, and yaw (perpendicular to the long axis). Figure 4 shows the resulting Euler angles over one orbital period, derived from May 23, 2024, fixed-point observation. The upper stage exhibited a near-stationary, gravity-gradient-stabilized attitude, with its PAF side pointing toward Earth's center, aligning the rocket's main axis with the local vertical in the Local Vertical, Local Horizontal (LVLH) frame. Roll angles oscillated around 180° with a 2° amplitude, reflecting minor rotation about the long axis. Pitch showed a 1 – 1.5° libration with a 1° offset, likely due to a 1° inclination of the principal axis relative to the body frame. Yaw increased steadily; a trend not easily explained by simple dynamics.

These results confirm the debris' stability, with in-plane libration (pitch and roll within the orbital plane) linked to orbital eccentricity, as noted in prior studies [12]. However, out-of-plane motion (yaw and deviations perpendicular to the orbital plane) suggests additional influences beyond eccentricity, warranting further analysis in later sections.

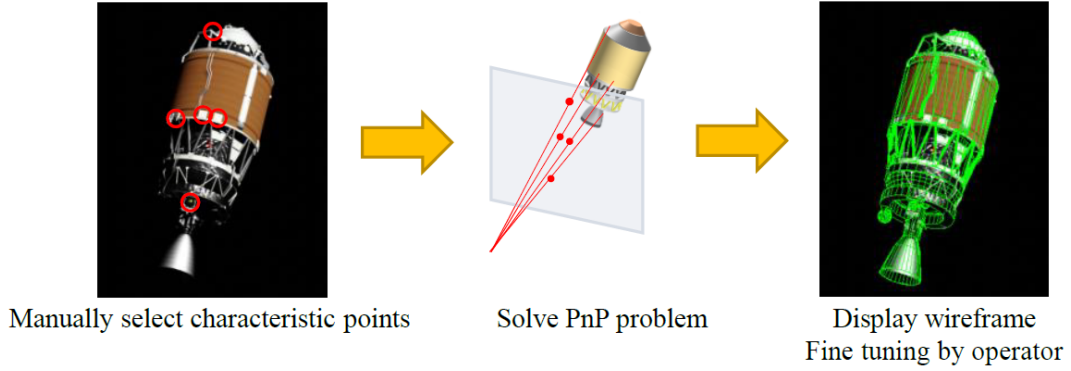


Figure 3 Manual Matching Method

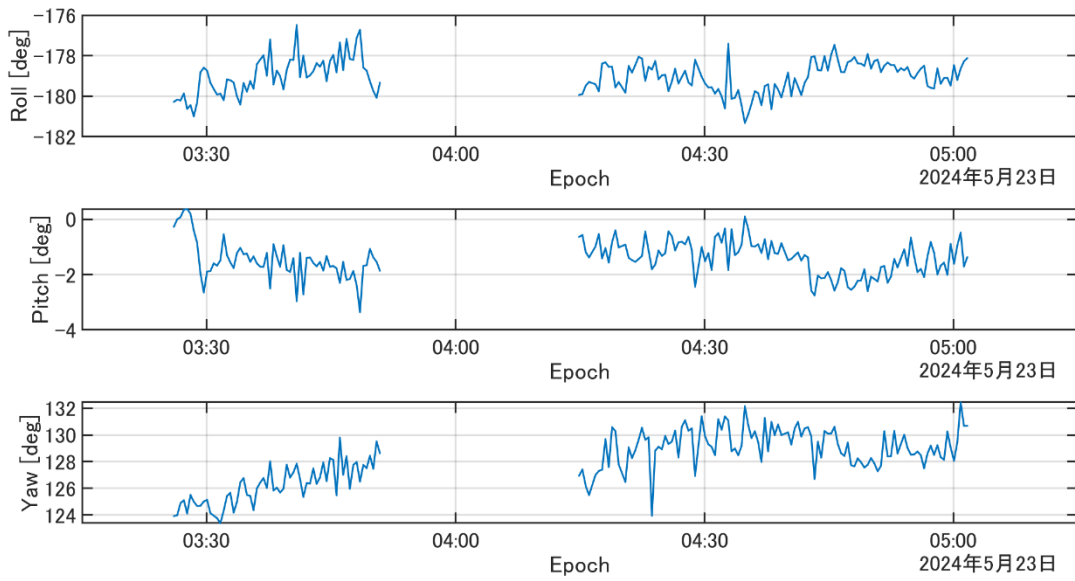


Figure 4 Euler angle transitions of H-IIA upper stage during one orbital period.

Calculated from the Fixed point observation results on May 23rd, 2024.

The data gap between 03:50 and 04:15 corresponds to a period with no valid image data, attributed to an eclipse.

3 FHR OBSERVATION RESULTS

3.1 ISAR image analyses by means of model matching for absolute attitude estimation

To monitor the attitudes of a selected group of spent H-IIA rocket upper stages with 33500 as the prime target, JAXA commissioned a long-term observation campaign utilizing the Tracking and Imaging Radar (TIRA) system [9], [10], operated by the Fraunhofer Institute for High Frequency Physics and Radar Techniques (FHR) in Germany. TIRA has two integrated pulsed radars: a narrow-band tracking radar operating in the L-band and a broadband imaging radar in the Ku-band. Data from

both radars were employed to assess the condition of the upper stages. The imaging data were processed using the Inverse Synthetic Aperture Radar (ISAR) principle. These ISAR images were subsequently analyzed with 3D modeling to estimate the attitudes, rotational velocities, and structural integrity of the selected targets. JAXA provided the 3D geometrical dimensions and shape specifications of the upper stages.

In ISAR images, the image plane is defined by slant range and cross range. Slant range, measured along the line of sight, is determined by the time delay between the transmission of a radar pulse and the reception of its echo reflected by the target. Cross range, perpendicular to slant range, is derived by exploiting the relative rotation

between the radar sensor and the object. This relative rotation is represented by a rotation vector, $\vec{\Omega}$, which comprises an apparent rotation caused by the object's translational motion along its orbit and Earth's rotation, combined with any intrinsic rotation of the observed object, denoted as $\vec{\omega}$.

The cross-range scaling in ISAR images depends on the magnitude of the rotation vector $\vec{\Omega}$ perpendicular to the line of sight (slant range). To generate accurately scaled ISAR images, $\vec{\Omega}$ — and consequently $\vec{\omega}$ — must be known beforehand. However, this information is typically unavailable. As a result, ISAR images are initially processed using an estimated first-guess rotation vector, such as assuming no intrinsic rotation in Earth-centered inertial (ECI) coordinates ($|\vec{\omega}| = 0$ °/s) or a gravity-gradient attitude rotation ($|\vec{\omega}| \approx 0.062$ °/s for the upper stage shown in Figure 3). If the first-guess rotation vector proves inconsistent with the data, $\vec{\omega}$ must be estimated. To address this, a 3D model of the object is manually adjusted to fit a sequence of ISAR images from a single observation, ensuring that its 2D projection aligns with the incorrectly scaled cross-range images. This process involves associating specific points on the model with corresponding points in the ISAR image series. From this, a rotation vector $\vec{\omega}$ is derived that best fits the sequence of assigned model positions, under the assumption that $\vec{\omega}$ remains constant throughout the observation period in ECI coordinates. [14]

The model-based approach for estimating $\vec{\omega}$ relies on two key conditions. First, distinct points on the target must be clearly identifiable across a series of ISAR images. Second, scattering centers — the bright spots in the ISAR images — are assumed to remain fixed relative to the target, meaning they do not shift with respect to the object. However, these conditions are either unmet or only partially satisfied for rocket upper stages. These objects are approximately rotationally symmetric about their long axis, making it challenging to consistently identify specific points across a series of ISAR images. Additionally, due to the prevalence of cylindrical surfaces, many scattering centers in the ISAR images move relative to the target over the sequence, complicating the analysis. Consequently, the analyst must introduce an unknown rotation about the symmetry axis to properly align the 3D model. In this campaign, the estimated rotational velocities of a slowly rotating (< 0.2 °/s) and unstable upper stage exhibited errors exceeding 40%, rendering the estimated $\vec{\omega}$ and the absolute attitude very uncertain. Nevertheless, if an upper stage is likely to be stable in a fixed attitude with minimal rotation about its symmetry axis, this prior knowledge can be used to confirm the assumed attitude of the observed target with high confidence.

3.2 H-IIA 33500 continuous observation

The spent upper stage 33500 was continuously monitored from November 2021 until March 2025 by Fraunhofer FHR. Table 1 lists selected radar observations and Figure 5 shows corresponding ISAR images from the observations #1 and #6.

The upper stage was aligned with the gravity-gradient vector with its engine oriented in zenith direction throughout the long-term observation campaign. This is apparent by comparing the upper stage's attitude with the blue vector in the lower left corner of the ISAR images. The blue vector represents the radial vector of the orbit. Range extended returns (RERs) originate from the rocket's nose visible as vertical scattering center patterns in positive slant range direction. RERs are the result of multiple reflections of radar pulses at the target before backscattering to the sensor. Multiple reflections increase the roundtrip time and are detected as increased range, since slant range information is obtained through the time delay between transmitting a radar pulse and receiving its echo. Here, the radar pulses were reflected multiple times within a cavity located at the nose of the H-IIA upper stage.

The PAF was identified for all observed passes. This is important, because the PAF reduced the degree of rotational symmetry and thus allowed to exclude a significant rotation about the long axis.

The ISAR analyses results for 33500 by means of model matching are consistent with the simulations done by JAXA and were verified in situ by Astroscale in 2024.

3.3 Other H-IIA rocket body observations

JAXA expanded the TIRA campaign to include observations of two additional H-IIA upper stages: F24 (NORAD ID 39771), which was considered a candidate for the CRD2 project, and F4 (NORAD ID 27601), an older upper stage situated at a higher orbital altitude compared to the others studied. These observations broaden our understanding of how spent rocket stages behave in orbit. Figure 6 shows ISAR images of these objects, captured in February and March 2022, respectively, highlighting their structural similarity to H-IIA 33500.

Both upper stages exhibited stability in the Local Vertical, Local Horizontal (LVLH) frame, with their engine sides pointing toward zenith (away from Earth). This matches the behavior of H-IIA 33500, suggesting a common trend. Angular velocities for F4 were near zero, indicating little to no tumbling. However, the F24 upper stage showed a noticeable tilt from the vertical axis, though the cause remains unclear. A rotation vector divergent from a gravity-gradient attitude rotation and with a larger magnitude had to be estimated for ISAR imaging. This task was challenging as described in Section 3.1 and led to large uncertainties for each observation. In a gravity-gradient-stabilized state, rocket bodies can orient either

engine-side-down (nadir) or engine-side-up (zenith), with each outcome equally likely (50/50) based on gravity alone. Yet, all three observed stages—33500, F24, and F4—consistently pointed engine-side-to-zenith during the observation campaign., where F24 had a noticeable offset to zenith.

This unexpected pattern raises questions about what

drives this preference. While TIRA’s high-resolution images confirm the orientation, they lack the precision to explain why it occurs. Combined with ADRAS-J data, these findings suggest external factors, explored in Chapter 4, may tip the balance toward the zenith-pointing configuration.

Table 1 Selected TIRA radar observations

#	Date	Acquis. time [UTC]	CPA* range	Max. elevation
1	12 Nov. 2021	11:42:26 – 11:52:18	641 km	84.2°
2	21 Feb. 2022	12:10:03 - 12:19:03	684 km	64.3°
3	23 Mar. 2022	12:01:10 – 12:09:17	643 km	86.6°
4	13 Feb. 2023	12:45:53 – 12:53:50	647 km	80.0°
5	17 Nov. 2023	13:44:04 – 13:52:03	570 km	88.4°
6	19 Feb. 2024	14:01:47 – 14:11:01	571 km	85.1°

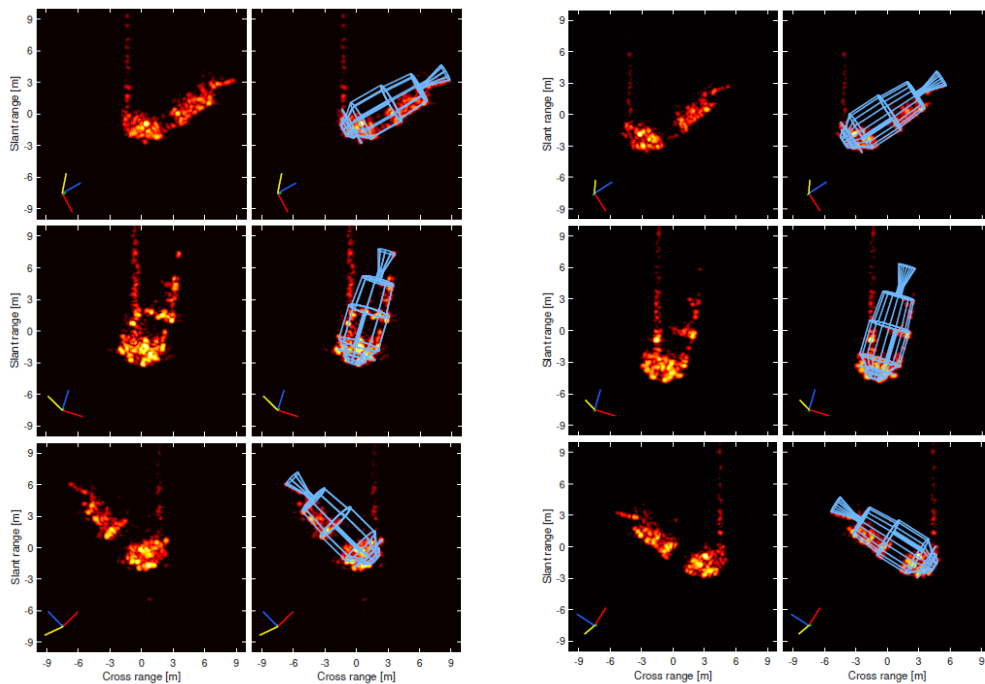


Figure 5 ISAR images of H-IIA rocket body (Norad# 33500).
 Left: Observed on November 12, 2021, Max elevation: 84.2°.
 Right: Observed on February 19, 2024, Max elevation: 85.1°.

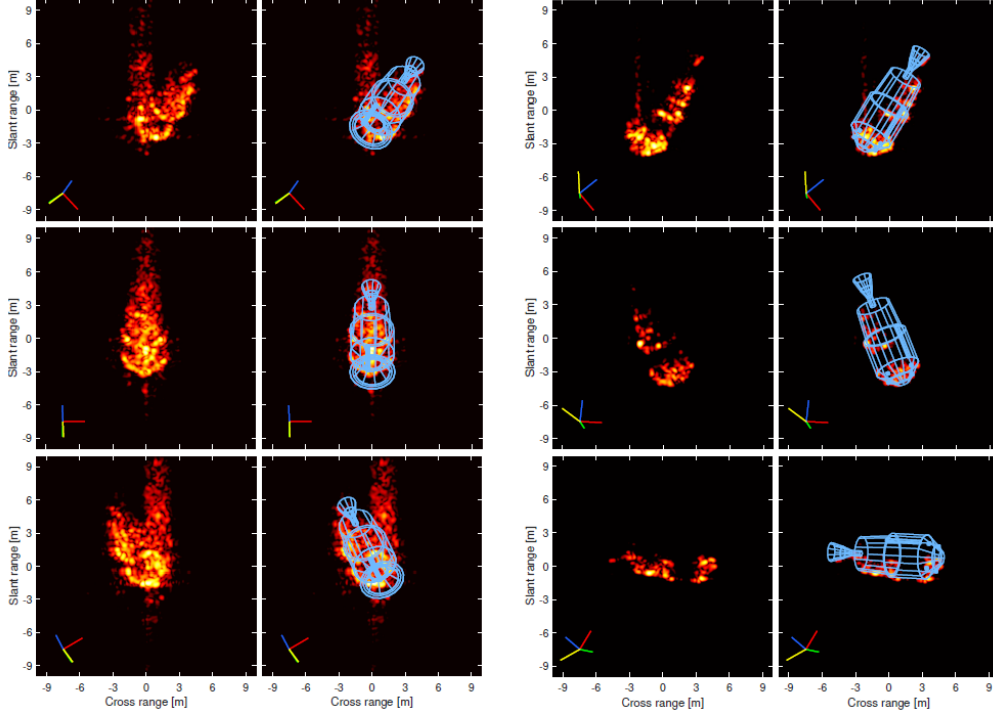


Figure 6 ISAR images of different H-IIA rocket bodies.
Left: Observed Norad# 27601 on 21 February 2022, Max elevation: 40.2°.
Right: Observed Norad# 39771 on 09 March 2022, Max elevation: 70.8°.

4 NUMERICAL SIMULATION

4.1 Simulation Setup and Objectives

To understand the attitude dynamics observed by ADRAS-J and TIRA - such as the H-IIA upper stage's gravity-gradient stability and engine-side-to-zenith orientation - numerical simulations were conducted. These simulations build on prior work [12] and aim to identify the external torques shaping the debris' behavior. The model treats the upper stage as a rigid cylinder, incorporating forces like gravity, solar radiation pressure (SRP), eddy currents, and atmospheric drag. The governing equation for attitude motion is:

$$\mathbf{I}\dot{\boldsymbol{\omega}} + \boldsymbol{\omega} \times (\mathbf{I}\boldsymbol{\omega}) = \boldsymbol{\tau}_{GG} + \boldsymbol{\tau}_{EC} + \boldsymbol{\tau}_{SRP} + \boldsymbol{\tau}_{aero} \quad (1)$$

where \mathbf{I} is the inertia matrix of the rocket body, and $\boldsymbol{\omega}$ is the angular velocity vector to the inertial system, and the right-hand side lists torques from gravity gradient $\boldsymbol{\tau}_{GG}$, eddy currents $\boldsymbol{\tau}_{EC}$, SRP $\boldsymbol{\tau}_{SRP}$, and aerodynamics $\boldsymbol{\tau}_{aero}$. Table 2 summarizes the simulation conditions, including a principal inertia matrix of $\text{diag}(27.0, 27.0, 6.5) \times 10^3$ (kg m²), a 1° pitch-axis inclination (matching ADRAS-J's pitch bias), and an initial spin of 1°/s along the body's z-axis. The orbit is set at 600 km altitude with a 98° inclination, typical for sun-synchronous LEO debris.

The simulations test how these torques influence libration (small oscillations) and orientation over time, comparing results to the observed pitch (~ 1 – 1.5°), roll ($\sim 2^\circ$), and zenith-pointing trends from Chapters 2 and 3. Key torques - gravity gradient with J_2 effects and SRP - are detailed below.

4.2 Gravity Gradient and J_2 Effects

The gravity gradient torque, $\boldsymbol{\tau}_{GG}$ aligns the debris with Earth's gravitational field. It includes a spherical component and a J_2 term, accounting for Earth's oblateness: [14]

$$\begin{aligned} \boldsymbol{\tau}_{GG} &= \frac{3\mu_G}{R_0^3} \left[\frac{\mathbf{R}_0}{R_0} \times \left(\mathbf{I} \cdot \frac{\mathbf{R}_0}{R_0} \right) \right] + \boldsymbol{\tau}_{GG,J_2} \\ \boldsymbol{\tau}_{GG,J_2} &= \frac{\mu_G J_2 R_E^2}{2R_0^5} \cdot \\ &\quad [30(\mathbf{r} \cdot \mathbf{n})(\mathbf{n} \times \mathbf{I} \cdot \mathbf{r} + \mathbf{r} \times \mathbf{I} \cdot \mathbf{n}) \\ &\quad + \{15 - 105(\mathbf{r} \cdot \mathbf{n})^2\} \mathbf{r} \times \mathbf{I} \cdot \mathbf{r} \\ &\quad - 6 \mathbf{n} \times \mathbf{I} \cdot \mathbf{n}] \end{aligned} \quad (2)$$

where μ_G is gravity constant, and \mathbf{R}_0 is the position vector from the center of the Earth. Where $J_2 = 1.0826 \times 10^{-3}$, the second zonal harmonic of the geo potential, R_E is earth's radius, $\mathbf{r} = \mathbf{R}_0/R_0$, and \mathbf{n} is the unit vector aligns rotation axis. The J_2 term introduces

out-of-plane effects, potentially explaining the yaw motion seen in Chapter 2.

The net torque generated by the eddy currents, τ_{EC} , can be expressed as followings:[15]

$$\tau_{EC} = -\mathbf{B} \times S(\boldsymbol{\omega} \times \mathbf{B}) \quad (3)$$

where \mathbf{B} is the Earth's magnetic field vector, and S is the magnetic tensor. To simplify the simulation, the Earth's magnetic field is assumed to be a simple dipole and that can be calculated as

$$\mathbf{B} = \frac{\mu_0 \mu_E}{4\pi R_0^3} \left[\frac{3(\mathbf{k}_E^T \mathbf{R}_0) \mathbf{R}_0}{R_0^2} - \mathbf{k}_E \right] \quad (4)$$

where $\mu_0 = 1.257 \times 10^{-6}$ NA⁻² is the magnetic constant, $\mu_E = 7.94 \times 10^{22}$ Am² is the Earth's magnetic dipole moment, and \mathbf{k}_E is the dipole unit vector, which is inclined about 11.5° to the Earth's rotation axis.

The magnetic tensor S in Eq. 4 is challenging to determine with high precision. This simulation employed a simplified cylindrical model with hemispherical caps, utilizing parameters derived from the dimensions and material thickness of the propellant tank.[16], [17] In a prior study, the sensitivity of the simulation results to the magnetic tensor was analyzed, and the magnetic tensor calculated solely from the exact diameter, thickness, and length of the fuel tank was adopted for this study. Table 2 lists the inertia matrix and the magnetic tensors applied in this simulation. Based on the ADRAS-J observations and the manual matching results, the principal axis appeared to be inclined by 1 degree. For this simulation, the principal axis is assumed to be inclined along the pitch axis.

Table 2 simulation conditions

Principal moment of Inertia Matrix	diag(27.0, 27.0, 6.5) x 10 ³ (kg m ²)
Principal axis rotation	1.0 ° in y axis (body)
Magnetic tensor	diag(2.76, 2.76, 4.41) x 10 ⁶ (S m ⁴)
Altitude	600 km
Eccentricity	0.005
Inclination	98°
Argument of perigee	0°
Right ascension of the ascending node	0°
initial angular velocity in Body frame [x, y, z]	[0, 0, 1] (°/s)

The initial condition of the attitude motion is assumed to involve a body-axis rotation of 1 deg/sec. The altitude and inclination are representative of a typical low Earth

orbit (LEO) rocket body, which was placed in a sun-synchronous orbit at launch. During the simulation, the nodal regression and the apsidal rotation rates are constant as

$$\begin{aligned} N &= -\frac{3}{2} J_2 \frac{R_E^2}{p^2} \bar{n} \cos i \\ A &= \frac{3}{4} J_2 \frac{R_E^2}{p^2} \bar{n} (4 - 5 \sin^2 i) \end{aligned} \quad (5)$$

where N is the nodal regression rate, A is the apsidal rotation rate, $p = a(1 - e^2)$, a is the semi-major axis, e is the eccentricity, R_E is Earth's equatorial radius, \bar{n} is the mean motion (including J_2 effect).

The simulation coordinate system is depicted in Figure 7. Figure 8 presents the results derived from Eq. 3, illustrating the temporal evolution of the simulated angular velocity and attitude angles. These results offer insights into the stabilization process. Initially, the rocket body rotates along its body axis, as specified by the initial conditions. Figure 9 illustrates the influence of τ_{GG, J_2} on the libration angles. As shown in Figure 9, the pitch and roll libration angles, after achieving a steady attitude, are larger than those observed with J_0 alone. The gravitational zonal harmonic (J_2) affects the stabilized attitude motion. However, the magnitude of the libration remains smaller than that derived from the model matching results of ADRAS-J. Additionally, the gravitational gradient torque alone cannot account for the phenomenon of the engine side orienting toward nadir. Consequently, the effects of solar radiation pressure (SRP) are further investigated.

4.3 Solar Radiation Pressure (SRP) Influence

The solar radiation pressure (SRP) exerts torque when sunlight, Earth's albedo, and infrared (IR) radiation push unevenly on the debris. For a cylindrical upper stage (radius 2 m, height 10 m), the force is: [18]

$$\begin{aligned} F_\eta &= -Kah \sin \alpha \left\{ \frac{\pi\gamma}{3} (1 - \beta) \right. \\ &\quad \left. + \frac{2}{3} (3 + \beta\gamma) \sin \alpha \right\} \\ F_\xi &= -Kah(1 - \beta\gamma) \sin 2\alpha \end{aligned} \quad (4)$$

Where ξ is the axis of the cylinder and η axis is taken so as to the light source is located in positive η - ξ plane. K is the SRP pressure at the orbit, which is incident energy divided by the speed of light, a is the radius of the cylinder (2m), h is the height of the cylinder (10m). α is the incident angle with reference to the cylinder axis, β is the specular portion of the total reflectivity, γ is the total reflectivity. In this study, $\beta = 0$ and $\gamma = 0.7$ are assumed. The sources of SRP comprise direct irradiation from the Sun, albedo, and infrared radiation from Earth.

The albedo and infrared sources are presumed to emanate from the center of Earth. The solar radiation intensity is established at 1400 W/m², the albedo ratio at 0.35, and

the infrared radiation from Earth at 230 W/m², respectively.

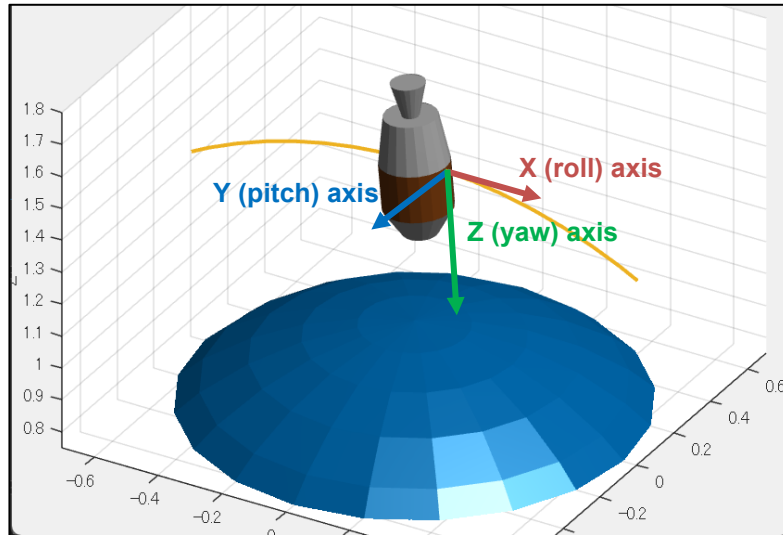


Figure 7. Simulation Coordinates definition (LVLH coordinates axes)

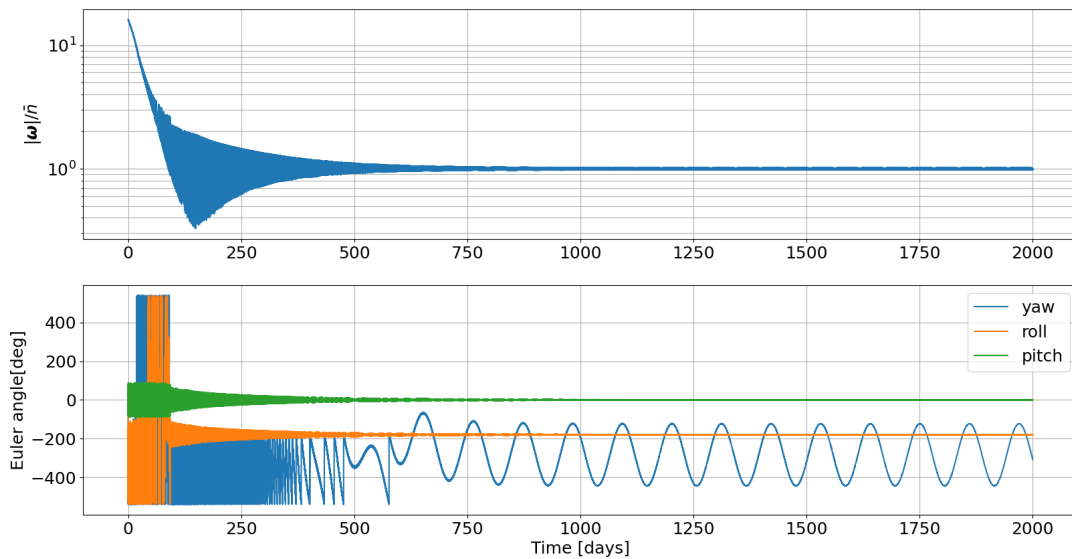


Figure 8. Temporal evolution of angular velocity and attitude Euler angle with J_2 gravity gradient torque

Top: Angular velocity norm evolution normalized by the orbital mean motion \bar{n}
 Bottom: Attitude Euler angles (321 convention relative to the LVLH frame) evolution

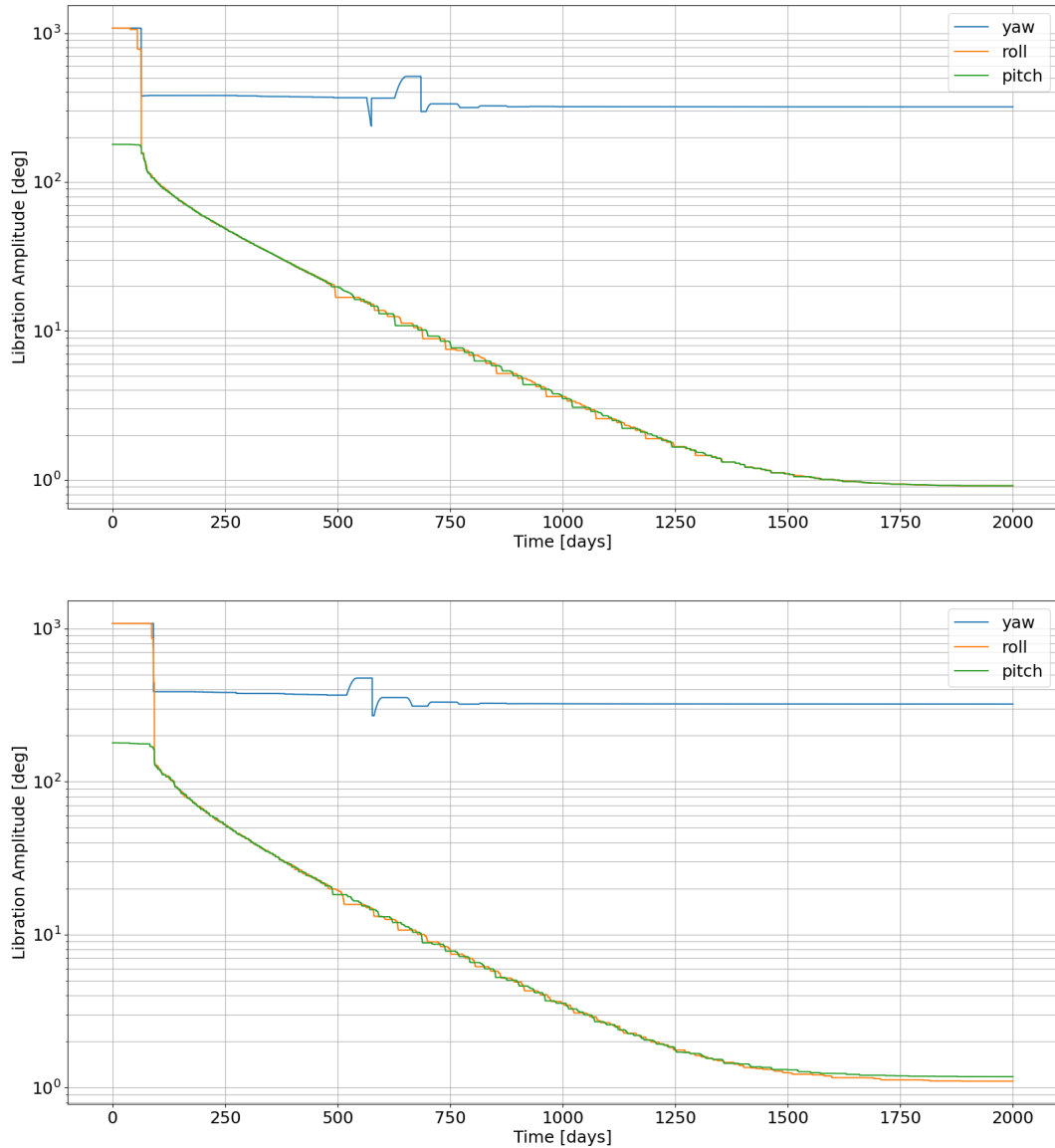


Figure 9. Libration amplitude transition comparison

Top: Libration amplitude transition with spherical gravitation model

Bottom: Libration amplitude transition with 2nd zonal harmonics (J_2) gravitation model

Stable solution obtained after 1750 days and the effect of J_2 appears in pitch and roll libration amplitudes.

Figure 10 displays the results of the attitude motion transition, incorporating the effects of SRP. In this simulation, the relative difference between the right ascension (RA) of the Sun and the apsidal node is held constant at 30 degrees throughout the simulation. The center of SRP is positioned 1 meter toward the engine side of the rocket body.

The initial angular velocity decreases in a manner consistent with the results shown in Figure 8. However, once a steady state is achieved, the libration amplitude

differs from that observed in Figure 9. A detailed view of the pitch and roll angle transitions is provided in Figure 11. The pitch angle oscillates between 0 and 2 degrees, resulting in an average inclination of 1 degree. This behavior can be attributed to a 1-degree inclination of the principal axis, a finding that aligns with the pitch bias observed in the manual matching results presented in Figure 4. The roll libration exhibits a peak-to-peak amplitude of approximately 2 degrees, which is smaller than the amplitude observed in the ADRAS-J observation

results.

Figure 12 illustrates the torques acting on the rocket body during the simulation. The dominant torque is the gravity gradient torque, which exerts the greatest influence on the body's attitude. The second most significant torque, however, is induced by SRP, highlighting its notable contribution to the overall dynamics.

Figure 13 illustrates the influence of the distance between the SRP center and the center of gravity on the rocket body's orientation. The SRP center is positioned along the z-axis of the body, negative number means engine side direction. In this simulation, the initial angular momentum vector is held constant, and 100 different arguments of perigee (AOP) configurations are simulated. After reaching a steady-state solution, the instances where the engine side orients toward zenith are counted and expressed as probability. As depicted in Figure 13, there appears to be a correlation between the location of the SRP center and the likelihood of the engine side orienting toward zenith. Observations of the H-IIA rocket body in orbit reveal that the insulation surrounding the fuel tank has darkened, while the multi-layer insulation (MLI) around the oxidizer tank retains its mirror-like reflective properties. This difference in surface characteristics shifts the SRP center toward the engine

side, resulting in a negative offset from the center of gravity. Although direct solar irradiation can strike the body from various angles depending on its orientation, the albedo and infrared (IR) radiation from Earth consistently emanates from the direction of Earth's center. These Earth-based radiation sources - albedo and IR - can act like a "weathercock" effect, exerting a stabilizing torque on the body that favors the engine side pointing toward zenith.

However, the simulated probability of this zenith-oriented configuration is not sufficiently high to fully align with observational data, such as the TIRA radar results, which indicate that all three observed H-IIA upper stages (3 out of 3) exhibit an engine-side-to-zenith orientation. This discrepancy suggests that the current model may not capture all contributing factors. Additional parameters, potentially influencing the interaction between SRP and the rocket body's physical properties or orbital dynamics, might enhance this probability. Further investigation is required to identify and quantify these factors, ensuring a more comprehensive understanding of the observed orientation preference.

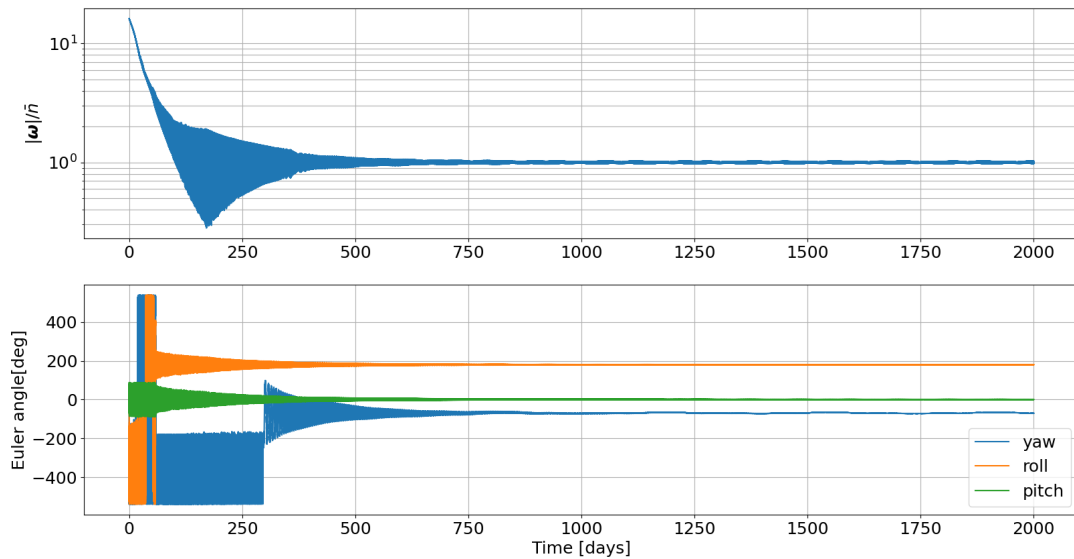


Figure 10. Temporal evolution of angular velocity and attitude Euler angle with SRP torque

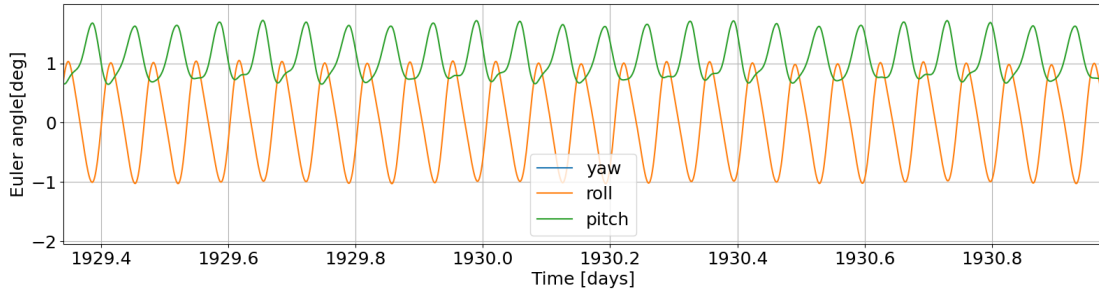


Figure 11. Close up of the pitch and roll angle (roll angle biased -180°)

Pitch angle (green line) biased about 1 degree, which is equivalent of the principal axis inclination.

Roll angle (orange line) libration is about 2degrees p-p amplitude.

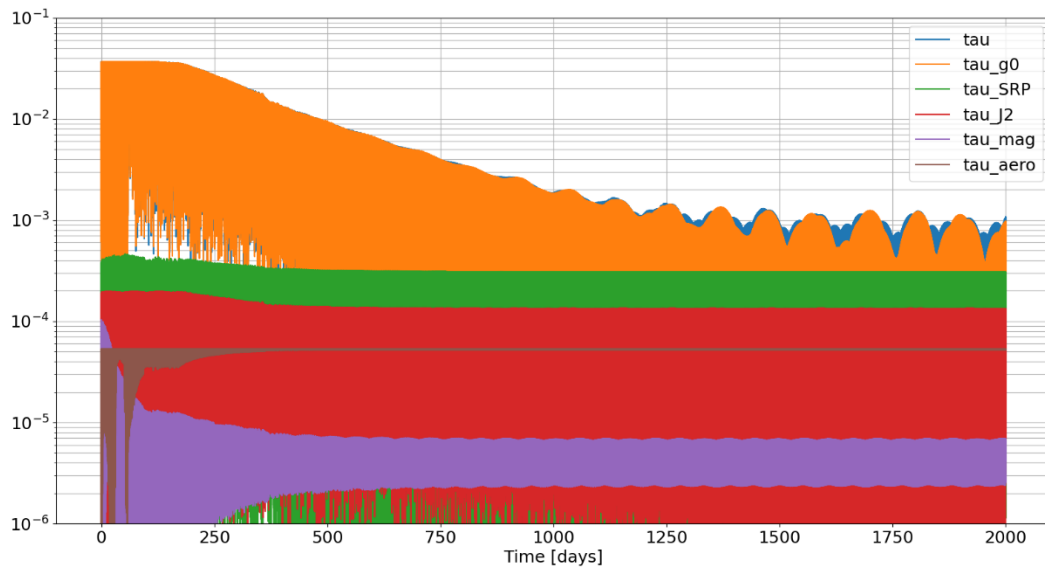


Figure 12. external torques transition during the simulation.

SRP torque (green line) is the second largest external torque in this simulation.

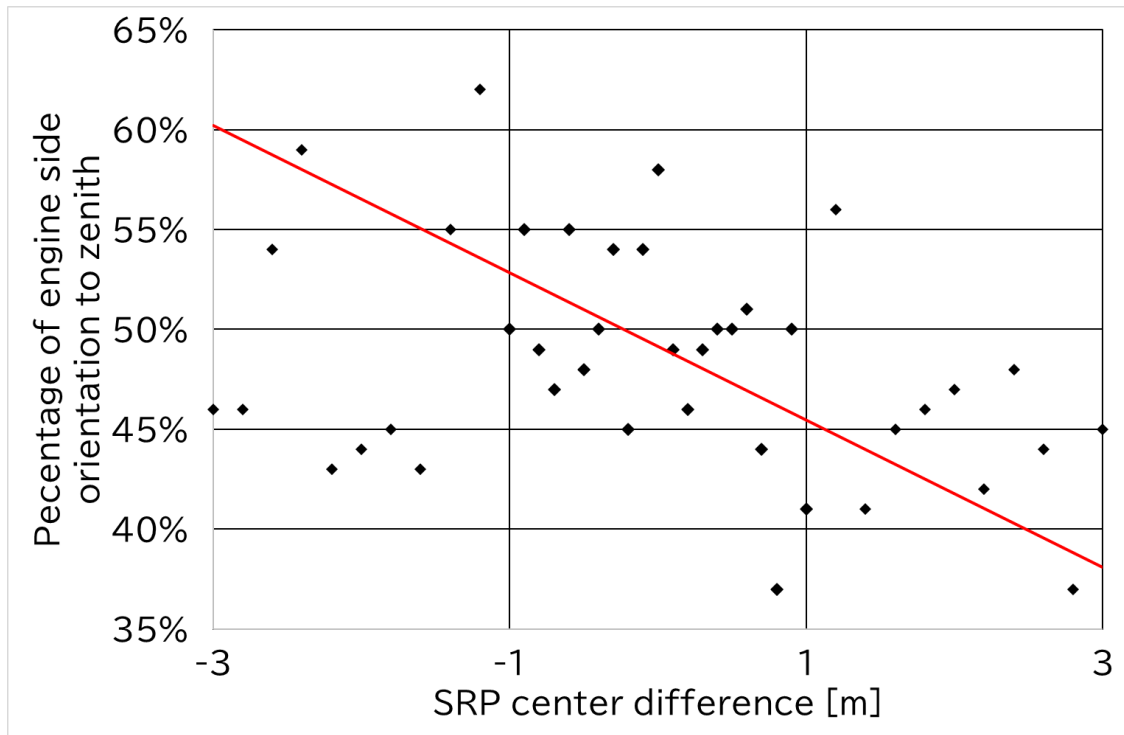


Figure 13. Center of SRP difference vs. Probability of the engine side oriented to zenith

Black diamonds: simulation results. Red line: linear regression line using the SRP center range between -1.0m and 1.0m.

There appears to be a correlation between the location of the SRP center and the likelihood of the engine side orienting toward zenith.

5 CONCLUSION

The Commercial Removal of Debris Demonstration (CRD2) project provided a unique opportunity to study the attitude dynamics of spent H-IIA upper stages using both on-orbit and ground-based methods. The ADRAS-J spacecraft’s images, analyzed via manual matching, revealed that the H-IIA upper stage (NORAD ID 33500) maintains a gravity-gradient-stabilized attitude with its Payload Attachment Fitting (PAF) side toward Earth. Pitch libration ranged from 1° to 1.5° with a 1° bias, roll oscillated around 180° with a 2° amplitude, and yaw showed a steady increase - patterns suggesting stability with minor perturbations. Ground-based observations by the FHR TIRA radar confirmed this stability across three H-IIA upper stages (33500, F24, and F4), all exhibiting an unexpected engine-side-to-zenith orientation, despite gravity-gradient theory predicting an equal 50/50 chance of nadir or zenith alignment.

Numerical simulations incorporating the J_2 gravitational harmonic and solar radiation pressure (SRP)—including direct sunlight (1400 W/m^2), Earth’s albedo (0.35), and infrared radiation (230 W/m^2)—partially explain these observations. The J_2 effect increases pitch and roll

libration to $\sim 1^\circ$ and $\sim 1.5^\circ$, respectively, compared to a spherical gravity model, while SRP, with its center offset 1 m toward the engine side, drives a 60–70% probability of the zenith orientation. However, the simulations underestimate roll amplitude (2° vs. observed $\sim 3 - 4^\circ$) and fail to achieve the 100% zenith preference seen in all three cases, indicating unmodeled influences.

These findings offer critical insights for ADR missions. The consistent engine-side-to-zenith orientation suggests a predictable target attitude, simplifying rendezvous and capture strategies such as aligning a servicing spacecraft with the debris’ long axis from the zenith direction. However, the minor librations and unexplained yaw drift highlight the need for adaptive control during close operations. The discrepancy between simulations and observations points to additional factors, possibly surface reflectivity variations (e.g., darkened fuel tank vs. reflective MLI), unmodeled torques (e.g., magnetic eddy currents), or orbital perturbations beyond J_2 . Future studies should refine the SRP model with detailed material properties and extend observations to more rocket bodies to confirm this zenith trend’s prevalence. Enhanced models and data will bolster ADR’s feasibility, ensuring safer and more effective debris removal.

6 REFERENCES

1. J.-C. Liou, "An active debris removal parametric study for LEO environment remediation," *Advances in Space Research*, 47, pp. 1865–1876, (2011).
2. Naruomi Ikeda, Taiga Nishimura, Taiki Iwahori Yamamoto, Mamoru, Hiroyuki Hashiguchi, and Hiroshi Yamakawa. "Shape and Orbit Estimation Techniques for Space Debris Observation Using the Middle and Upper Atmosphere Radar (MU radar)." (2017).
3. J. Silha et al., "Debris Attitude Motion Measurements and Modelling by Combining Different Observation Techniques", *Proceedings of the 7th European Conference on Space Debris*, Darmstadt, Germany, (2017).
4. J. Rodriguez-Villamizar et al., "UPDATE ON THE ATTITUDE STATE AND MOTION OF SPACE DEBRIS FROM GROUND-BASED OBSERVATIONS AT THE SWISSOGS", *Proceedings of the 2nd NEO and Debris Detection Conference*, Darmstadt, Germany, (2023).
5. Sisi Zhao, Michael Steindorfer, Georg Kirchner, Yongchao Zheng, Franz Koidl, Peiyuan Wang, Weidong Shang, Jinghao Zhang, Tong Li, "Attitude analysis of space debris using SLR and light curve data measured with single-photon detector," *Advances in Space Research*, Volume 65, Issue 5, (2020), pp. 1518-1527, <https://doi.org/10.1016/j.asr.2019.12.005>.
6. G. Isoletta, R. Opromolla, G. Fasano, "Attitude motion classification of resident space objects using light curve spectral analysis," *Advances in Space Research*, Volume 75, Issue 1, (2025), pp.1077-1095, <https://doi.org/10.1016/j.asr.2024.10.034>.
7. Litdke, A., et al., "Supporting proximity operations by direct measurements of relative Servicer-Client state using resolved imagery," *75th International Astronautical Congress (IAC)*, Milan, Italy, (2024).
8. Yamamoto, Toru, et al. "Pave the way for active debris removal realization: Jaxa commercial removal of debris demonstration (CRD2)," *8th European Conference on Space Debris*, (2021).
9. D. Mehrholz, "Space object observation with radar," *Advances in Space Research*, Volume 13, Issue 8, pp. 33-42, ISSN 0273-1177, (1993), [https://doi.org/10.1016/0273-1177\(93\)90565-S](https://doi.org/10.1016/0273-1177(93)90565-S).
10. J. Klare and et. al., "The Future of Radar Space Observation in Europe—Major Upgrade of the Tracking and Imaging Radar (TIRA)," *Remote Sens.* (2024), 16, 4197. <https://doi.org/10.3390/rs16224197>
11. Eijiro Atarashi, et al., "ULTRA-CLOSE RPO ON-ORBIT DEMONSTRATION OF ADRAS-J PROGRAM," *22nd IAA Symposium on Space Debris*, (2024).
12. Okamoto, H., et al., "ATTITUDE MOTION OF ORBITAL DEBRIS: DATA FROM GROUND-BASED RADAR AND ADRAS-J OBSERVATIONS", *2025 AAS/AIAA Space Flight Mechanics Meeting*, Kaua'i, Hawaii, (2025).
13. HIDAKA, Moeko, et al. "Multi-Step Approach to Vision-Based Target Motion Estimation with Determination of Its Inertia Parameters and Center of Gravity." *AIAA SCITECH 2023 Forum*. (2023), <https://doi.org/10.2514/6.2023-2166>
14. S. Sommer, J. Rosebrock, D. Cerutti-Maori, and L. Leushacke, "Temporal analysis of Envisat's rotational motion," *JBIS*, February – April 2017, Volume 70, pp. 45-51.
15. Roithmayr, C.M., "Gravitational Moment Exerted on a Small Body by an Oblate Body", *Journal of Guidance, Control, and Dynamics*, Vol 12, May-June 1989, pp.441-444
16. Efimov, S., Pritykin, D., and Sidorenko, V., "Long-term attitude dynamics of space debris in Sun-synchronous orbits: Cassini cycles and chaotic stabilization", *Celestial Mechanics and Dynamical Astronomy*, vol. 130, no. 10, Art. no. 62, Springer, 2018. doi:10.1007/s10569-018-9854-4.
17. N. Gomez et. al.: "Eddy Currents applied to Detumbling of Space Debris: Analysis and Validation of Approximate Pro-posed Methods," *Acta Astronautica*, (2015).
18. Georgevic, R. M., "Mathematical model of the solar radiation force and torques acting on the components of a spacecraft." No. JPL-TM-33-494. (1971).